



Research article

Theoretical and experimental understanding of Li_2S crystal structure and its isotropic ion conduction mechanism

Ramkumar Balasubramaniam^{a,b}, Anjali Anilkumar^a, Joon-Hyung Lee^c, Yun-sung Lee^a, Sangho Park^{d,*}

^a School of Chemical Engineering, Chonnam National University, Gwangju 500 757, Republic of Korea

^b Department of Battery Engineering, Dongshindae-gil 34-22, Naju-si, Jeollanam-do 58245, Republic of Korea

^c Department of Renewable Energy, Dongshin University, Dongshindae-gil 34-22, Naju-si, Jeollanam-do 58245, Republic of Korea

^d School of Chemical Engineering, Jeonbuk National University, 567 Baekje-daero, Deokjin-gu, Jeonju-si, Jeonbuk State 54896, Republic of Korea



ARTICLE INFO

Keywords:

Carbothermal reduction method
Precursor material
Molecular Dynamics
Nudged Elastic Band
Ionic conductivity
Activation energy

ABSTRACT

Lithium sulfide is a crucial material for Li-S solid electrolytes, as it serves as the costly precursor in the research and development of solid-state batteries. This study introduces an economical carbothermal reduction method for synthesizing Li_2S powder. Physicochemical studies are conducted to assess the crystallinity, morphology, homogeneity, and oxidation state of the produced Li_2S powders. DFT calculations are utilized to visualize the crystal structure and atomic sites in Li_2S . Electrochemical impedance spectroscopy analysis examines the ionic conductivity of the prepared pellets at specific temperatures. NVT-Molecular Dynamics method is applied to evaluate the diffusion coefficient of Li_2S crystal structure at both low and high temperatures. A high concentration of disordered defects correlates with excellent ionic behavior at $T = 700$ K. The Nudged Elastic Band study demonstrates the activation energy (E_{Li^+}) for Li ion hopping between neighboring and distant Li sites. The low activation barrier and identification of lithium ion conduction channels confirm that Li_2S is an isotropic ionic conductor.

1. Introduction

Lithium ion batteries (LIBs) have garnered considerable attention due to their high energy density and outstanding electrochemical performances [1–3]. The utilization of sustainable, renewable energy storage devices has increased due to global warming and air pollution caused by petroleum products. The use of LIBs in portable and mobile devices such as smartphones, robots, drones, and transportation systems (for example, electric vehicles, hybrid electric vehicles) is rapidly increasing [4–6]. Nevertheless, current LIB cathodes, including LiCoO_2 , $\text{LiNi}_{1-x}\text{Co}_x\text{Mn}_x\text{O}_2$ ($x = 0-1$), and LiFePO_4 -based oxides, are limited by their comparatively low discharge capacities (< 240 mAh g^{-1}), which hinders the achievement of high specific energy densities in LIBs [1, 3–5]. Additionally, oxide-based cathode materials provide higher voltage, reasonable energy density, and long cycle life for LIBs. However, Co- and Ni-based compounds are expensive, scarce, and toxic, which limits their potential for next-generation LIBs. In contrast, sulfur-based conversion-type lithium sulfide (Li_2S) materials offer higher theoretical gravimetric capacities of 1166 mAh g^{-1} [4,7]. More

importantly, sulfur solid electrolytes have been explored as alternatives to oxide solid electrolytes, enabling fast lithium-ion conduction and excellent ionic conductivity due to the polarizable nature of S^{2-} anions [8–10]. Even though Li_2S has many advantages, it is moisture-sensitive, which limits its usage. This is one of the foremost challenges when handling sulfur-based materials. Moreover, lithium sulfide (Li_2S) is considered the major precursor and primary cost driver for sulfide solid electrolytes and next-generation cathode materials. The Li_2S is a fascinating material for both technological and scientific applications. Currently, the commercial Li_2S powder research-grade is extremely costly (approximately \$ 15,000 per kg) [11,12]. The exploration of new chemistries to enhance the energy density and safety of LIBs, and significant progress towards the commercialization of novel materials, has been made. Developing raw materials for electrodes and electrolytes that are both safer and more economical is equally important [13].

Several synthesis methods have been explored for the scalable production of Li_2S powder. Commonly used techniques include ball-milling, carbothermal reduction, sulfuration, chemical lithiation, and atomic layer deposition to prepare the Li_2S material [4]. The LiH and S

* Corresponding author.

E-mail address: shpark92@jnbu.ac.kr (S. Park).

<https://doi.org/10.1016/j.nxmte.2025.101305>

Received 20 June 2025; Received in revised form 25 September 2025; Accepted 3 October 2025

Available online 6 October 2025

2949-8228/© 2025 The Authors. Published by Elsevier Ltd. This is an open access article under the CC BY license (<http://creativecommons.org/licenses/by/4.0/>).

precursors undergo ball-milling in an inert (Ar or He) atmosphere to produce submicron-sized Li_2S powder [4,14]. Although this method is simple and economical, ball milling's major disadvantage is its lack of precise control over particle size and morphology [4]. Additionally, this method leads to the undesirable formation of agglomerates. In the Sulfuration method, lithium and sulfur are sealed together and heated at 300 °C to produce Li_2S [4]. Furthermore, hydrogen sulfide (H_2S) and carbon sulfide (CS_2) serve as precursors for producing nm and μm sized Li_2S [4,14,15]. Vapor-phase ALD uses gaseous precursors like Li tert-butoxide ($\text{LiOC}(\text{CH}_3)_3$) and H_2S to synthesize amorphous nm- Li_2S [4]. Some groups have used lithium naphthalenide in 1,2-dimethoxyethane and lithium ethoxide with H_2S gas to produce Li_2S nanocrystals [16,17]. Nonetheless, these nanocrystals tend to aggregate into larger clusters due to the surface charge of alkoxide precursors [17]. Compared to liquid and gaseous precursors, solid-state precursors such as Li_2CO_3 , CH_3COOLi , and LiOH are used to synthesize Li_2S powder at high temperatures under a flow of H_2S gas [4,17–19]. However, it is important to note that some Li and S precursors are hazardous and costly [4]. Chemical lithiation produces nm or μm size Li_2S using lithiation agents such as lithium triethylborohydride and lithium naphthalenide with sulfur [4,20,21]. Moreover, these lithiating agents are prohibitively expensive and highly reactive when exposed to air and other environments.

Compared to alternative synthesis techniques, the carbothermic reduction process provides a cost-effective and scalable route for the production of Li_2S nanocrystals. This method requires lower energy input than electrolysis and utilizes inexpensive carbon-based reducing agents. From an industrial manufacturing perspective, the process is readily scalable from laboratory-scale to large-scale production. Additionally, it offers flexibility in raw material selection, accommodating a range of particle sizes without compromising the quality of the final product. Moreover, precise control over reaction parameters such as temperature, pressure, and carbon-to-oxide ratio enables optimization of the process conditions, thereby enhancing the purity of the final product [22–24]. The mechanism of the carbothermic reduction method involves Li_2SO_4 initially reacting with adjacent carbon to release CO_2 gas and produce Li_2S powder [4,25–27]. F. Ye *et al.* prepared the $\text{Li}_2\text{S}/\text{CNT}$ composite at approximately 645 °C using $\text{Li}_2\text{SO}_4\cdot\text{H}_2\text{O}$ and PVA (carbon source) [28]. H.T. Kim *et al.* prepared the $\text{Li}_2\text{S}/\text{CNT}$ composite at 700 °C under an N_2 flow using PVP as a carbon source [28]. These works focus on the cathode electrode preparation for Li-S batteries. S. Kaskel *et al.* prepared the Li_2S nanoparticles at 820 °C under Ar gas using $\text{Li}_2\text{SO}_4\cdot\text{H}_2\text{O}$ and Ketjen black (carbon source) [25]. This procedure is time-consuming because it involves a ball milling process for an extended duration (4 h to 60 h) to mix the precursors.

In this work, we employed a carbothermic reduction method that circumvents the use of lithium metal, which is not only expensive but also highly reactive and challenging to handle safely. Furthermore, our approach eliminates the need for hydrogen sulfide (H_2S) gas, a toxic and corrosive reagent that raises significant safety and environmental concerns. Unlike several conventional methods, the carbothermic reduction strategy described herein is readily scalable and utilizes cost-effective lithium salts and carbonaceous materials as precursors. This study presents a cost-effective method for synthesizing lithium sulfide (Li_2S) powder and demonstrates their crystallographic and electrochemical properties. Li_2S powder is synthesized by reacting Li_2SO_4 with glucose using a carbothermic reduction method at high temperatures. High-resolution X-ray diffraction, field-effective scanning electron microscopy, and X-ray photoelectron spectroscopy were employed to assess the phase purity, crystallinity, morphology, homogeneity, and oxidation state of the prepared powders. The synthesized Li_2S powders were formed into pellets, and their ionic conductivity was analyzed using electrochemical impedance spectroscopy. Li_2S plays a critical role in battery research due to its fundamental material properties. The ionic conductivity, particularly the migration of Li ions in Li_2S , is crucial for its performance. This study also explores the chemistry of Li ion hopping

in the Li_2S crystal structure through molecular dynamics and the nudged elastic band method.

2. Experimental section

2.1. Synthesis of Li_2S powder

The synthesis process of lithium sulfide (Li_2S) is illustrated in Fig. 1. Lithium sulfate monohydrate ($\text{Li}_2\text{SO}_4\cdot\text{H}_2\text{O}$) was used as the lithium source and dissolved in deionized water at room temperature under magnetic stirring. Glucose was then added to the solution at a 1:1 molar ratio with respect to $\text{Li}_2\text{SO}_4\cdot\text{H}_2\text{O}$. After stirring at room temperature for 1 h, a transparent and colorless solution was obtained. The solution was gradually heated to 150 °C to evaporate the solvent, yielding a dark brown powder. This powder was pre-heated at 400 °C for 1 h to remove residual organic matter. During this step, glucose decomposed into carbon, which uniformly coated the Li_2SO_4 particles. Subsequently, the resulting powder was subjected to high-temperature treatment at 780 °C for 3 h under an argon atmosphere to induce carbothermic reduction and crystallization of Li_2S . In this step, the carbon coating served as a reducing agent, reacting with oxygen to form gaseous CO_2 , which was purged by the Ar flow. This thermal process yielded a white Li_2S powder suitable for further characterization.

The Li_2S powder formation mechanism is described as follows: [4,12,25,27]

$$\text{Li}_2\text{SO}_4\cdot\text{H}_2\text{O} (\text{s}) + \text{Glucose} (\text{s}) \rightarrow \text{Li}_2\text{S} (\text{s}) + x\text{CO}_2(\text{g}) \quad [x = \text{number of molecules; } y = 1,2]$$

The final product was collected and used for subsequent physicochemical and electrochemical analysis.

2.2. Physicochemical characterization

High-resolution X-ray diffraction (HR-XRD; Rigaku D/MAX Ultima III, Japan) was used to analyze the crystalline structure of the synthesized Li_2S powder. The measurements were conducted using $\text{Cu K}\alpha$ radiation ($\lambda = 1.54178 \text{ \AA}$) at an operating voltage of 36 kV and a current of 20 mA, over a 2θ range of 20° to 80°. The surface and cross-sectional morphologies of the Li_2S powder and compressed pellet were examined using field-emission scanning electron microscopy (FE-SEM; Hitachi S-4700/EX-200, Japan). Elemental composition and chemical state analyses were performed using X-ray photoelectron spectroscopy (XPS; MultiLab 2000, VG, UK).

2.3. Theoretical modeling and molecular dynamic simulations

The theoretical model of the Li_2S crystal was computed using the Quantum ESPRESSO software package, which employs an ultrasoft pseudopotential code [29–32]. The crystal structure input code for Li_2S was sourced from the open crystal database (<https://www.crystallography.net/cod/>) and the materials project database (<https://next-gen.materialsproject.org/>) [31–40]. The Generalized Gradient Approximation (GGA) exchange-correlation function was utilized to calculate the properties of the Li_2S crystal [29,30,41]. The electronic ground state of the Li_2S crystal was used to conduct Molecular Dynamics (MD) simulations at temperatures of 300, 500, and 700 K to analyze lithium ion mobility [29,30]. To estimate the activation energy for lithium ion migration, the Nudged Elastic Band (NEB) method was applied, providing insights into the potential energy barriers along lithium hopping pathways [29,30,41–44,47]. Two neighboring Li sites were identified, and a defect was introduced at one site. The procedure was then repeated for another site in the crystal structure, and the resulting data were combined to determine the activation energy for the specific ion jump. This approach was further applied to two additional Li-ion sites. All calculations were performed using the cubic Li_2S crystal structure with a lattice parameter of 5.708 Å, containing only Li and S atoms. The electronic convergence criterion was set to 2.4×10^{-9} .

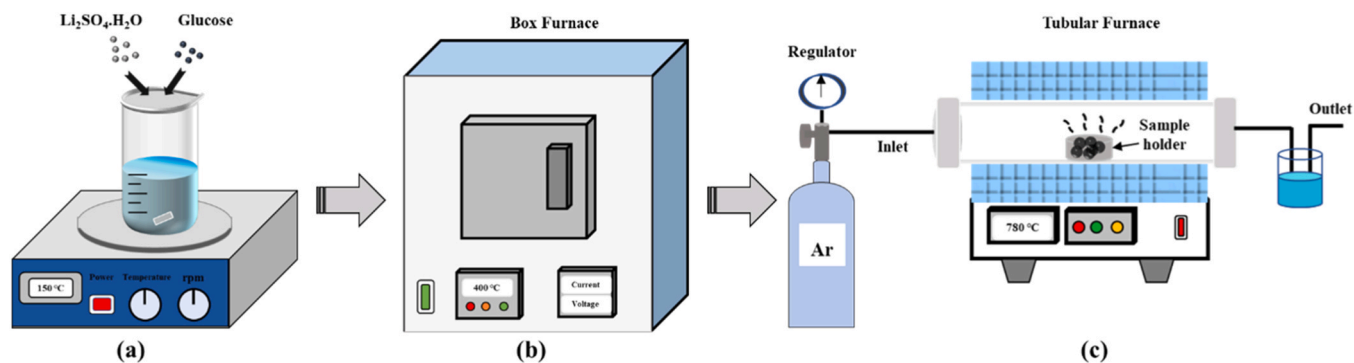


Fig. 1. Schematic diagram for the Li_2S powder synthesis process. (a) Stirring the precursors, (b) Carbonization process at 400 °C for 1 h under an air atmosphere and (c) Calcination process at 780 °C for 3 h under an argon atmosphere.

2.4. Electrochemical characterization

To evaluate the ionic conductivity of Li_2S , test cells were fabricated using 240 mg of Li_2S powder. The powder was uniaxially pressed into pellets under a pressure of 360 MPa. The resulting pellets were placed directly onto carbon-coated aluminum foil, which served as ion-blocking electrodes. Electrochemical impedance spectroscopy (EIS) was conducted using a VSP Bio-Logic system (France) over a frequency range of 1 MHz to 100 Hz at temperatures of 60 °C and 80 °C. Prior to measurement, each cell was equilibrated at the target temperature for 30 min to ensure thermal stability.

The ionic conductivity (σ) was determined using the equation: [1–3, 5]

$$\sigma = \frac{t}{R \times A}$$

Where σ represents the ionic conductivity (S cm^{-1}), R is the resistance (Ω), t is the thickness (cm), and A is the contact area (cm^2) of the cold-

pressed pellet with the ion-blocking electrode. The thickness of the pellet is approximately 1.027 mm, and the contact radius between the pellet and the current collector was 0.475 cm, yielding a contact area 0.708 cm^2 . The chronoamperometry (CA) of the Li_2S pellet was studied using ion-blocking and non-ion-blocking electrodes under an applied voltage of 1 V for a duration of 90 min. A 0.2 g sample of Li_2S powder was used to make a pellet under a pressure of 300 MPa. Indium foil was then attached to both sides of the pellet under the same pressure. The solid-state cell setup (ion-blocking cell) was subsequently used to measure EIS and chronoamperometry at 60 °C and 80 °C. A similar method was used to prepare the non-ion-blocking cell (Li symmetric cell). A pressure of 30 MPa was applied to attach the Li metal to the Li_2S pellet. The solid-state cell was used to measure resistance and current using a VSP Bio-Logic system (France).

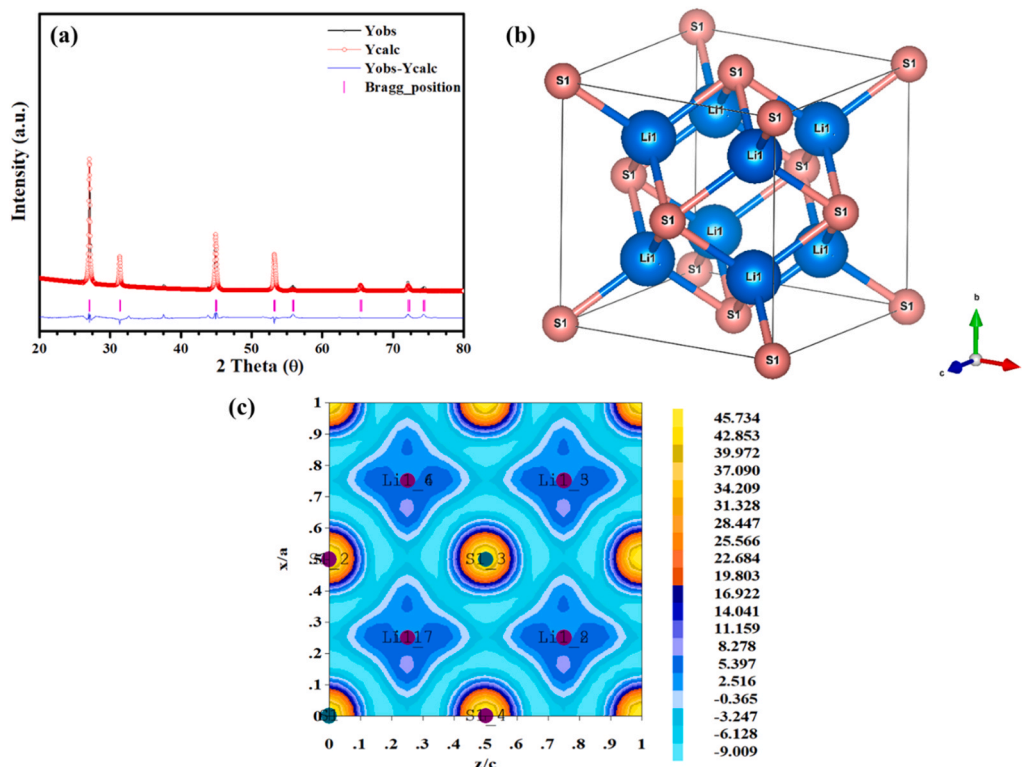


Fig. 2. (a) Rietveld refinement XRD pattern of Li_2S prepared at 780 °C for 3 h, (b) Crystal structure of the Li_2S , and (c) 2D Electron density map of the crystal structure.

3. Results & discussion

3.1. Physio-chemical properties

X-ray diffraction (XRD) analysis was employed to determine the phase composition, crystal structure, and lattice parameters of the prepared materials, as these factors directly influence their ionic conductivity. Fig. 2(a) presents the X-ray diffraction (XRD) pattern of the synthesized Li_2S powder, exhibiting sharp and well-defined peaks that confirm its high crystallinity. The diffraction pattern matches the standard reference for the cubic phase with space group Fm-3m (No. 225) [33–38,40], indicating that the synthesized sample is phase-pure with no detectable impurities. The calculated interplanar spacings (d-spacings) are 3.2959 Å, 2.8543 Å, 2.0183 Å, and 1.7212 Å, corresponding to the (111), (200), (220), and (311) planes, respectively. Fig. 2(b) provides a three-dimensional representation of the Li_2S crystal structure. The calculated lattice parameter for the cubic phase is $a = 5.7087$ Å, and the unit cell volume is 186.0452 Å³, which is in good agreement with previously reported values [33–38]. The average crystallite size of the synthesized material was estimated to be approximately 52 nm using the Scherrer equation. In addition, Fig. 2(c) presents a two-dimensional electron density distribution map derived from DFT calculations, illustrating the spatial localization of Li 1s and S 2p orbitals. The electron density is primarily concentrated around the sulfur atoms, with lower density regions around the lithium ions, confirming the ionic character of the Li–S bonding.

Fig. 3 illustrates the theoretically optimized crystal structure of Li_2S , comprising eight lithium atoms and four sulfur atoms within the unit cell. In this configuration, lithium ions (Li^+) occupy the 8c Wyckoff positions, while sulfur ions (S^{2-}) are located at the 4a sites. The calculated lattice parameter for the cubic phase is $a = 5.708$ Å, and the corresponding unit cell volume is 185.9738 Å³, which shows excellent agreement with the experimentally determined values [33–38].

As shown in Fig. 4, field-emission scanning electron microscopy (FE-SEM) images taken at various magnifications reveal that the Li_2S particles are relatively coarse, with an average particle size of approximately 7 µm. Notably, surface cracks are observed across many particles, which are likely attributed to the release of CO_2 during high-temperature processing at 780 °C. These structural features may influence the ionic transport and pelletization behavior of the synthesized Li_2S powder. Nevertheless, SEM analysis is crucial as it provides insights into the microstructure, porosity, cracks, voids, and surface roughness of the sample, all of which strongly influence the ionic conductivity of the prepared material.

Fig. 5 presents FE-SEM images of the Li_2S pellet at various magnifications. Fig. 5(a) displays a cross-sectional view of the pellet, revealing a measured thickness of approximately 1.027 mm and demonstrating a

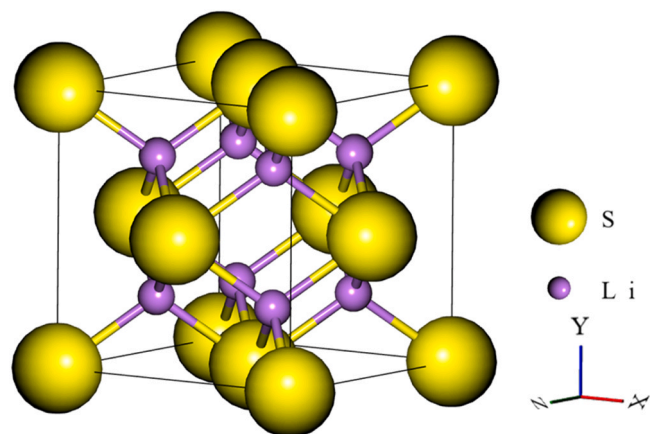


Fig. 3. Crystal structure of theoretically calculated Li_2S material.

compact and uniform structure. Fig. 5(b–d) depict the surface morphology and microstructure, where densely packed and well-connected Li_2S particles are evident. This microstructural integrity is expected to facilitate enhanced ionic conductivity by enabling continuous Li^+ migration pathways. Additionally, X-ray photoelectron spectroscopy (XPS) analysis was conducted to investigate the oxidation states of the constituent elements in the Li_2S powder. However, the identification of chemical states, surface composition, and surface chemistry is critical for achieving high ionic conductivity in the prepared materials.

Fig. 6 presents the X-ray photoelectron spectroscopy (XPS) analysis of Li_2S synthesized at 780 °C. The Li 1s core-level spectrum (Fig. 6a) exhibits a binding energy peak at 54.3 eV, while the S 2p spectrum (Fig. 6b) shows a peak centered at 160.3 eV. These values are consistent with previously reported results [21,45,46], thereby confirming the presence of Li–S bonding in the synthesized material. The fitted spectra align well with the experimental data, indicating a high degree of chemical purity and the expected oxidation states of lithium and sulfur. In addition, a small amount of residual carbon was detected in the prepared Li_2S . To address this issue, a solvent-leaching method is currently under development to effectively remove carbon impurities. Looking ahead, we aim to synthesize highly pure Li_2S powders suitable for next-generation electrochemical applications. Furthermore, complementary computational approaches are being employed to provide deeper insights into the structure–property relationships of Li_2S , particularly in relation to diffusion coefficients and activation energies.

3.2. Li-Ion conduction mechanism in the Li_2S crystal

MD trajectories capture the real-time motion of Li^+ ions, enabling the prediction of diffusion coefficients, which are critical for the performance of Li-ion conductors. The NVT-Molecular Dynamics results for the Li_2S crystal structure are exhibited in Fig. 7, Fig. 8a and Video V1–3. Each image captures the migration of lithium ions at specific time intervals. The trajectory images clearly verify the movement of lithium ions from their initial positions during the process. The total relaxation time for the NVT-MD simulation was 1 ps. Following the migration process, the calculated diffusion coefficients for the Li_2S crystals were $6.9875 \times 10^{-7} \text{ cm}^2 \text{ s}^{-1}$, $7.6875 \times 10^{-7} \text{ cm}^2 \text{ s}^{-1}$, and $1.1687 \times 10^{-6} \text{ cm}^2 \text{ s}^{-1}$ at temperatures of 300 K, 500 K, and 700 K, respectively (Fig. 8b). As the temperature increased, the diffusion coefficient (D_{Li^+}) of the Li_2S crystal also rose. Fig. 8c illustrates the Arrhenius plot of the Li_2S crystal at varying temperatures. At lower temperatures, the activation energy was 0.165 eV, decreasing to 0.029 eV at higher temperatures due to the proximity to its melting point (~ 938 °C) [4].

Figures S1 and S2a present the NVT molecular dynamics (MD) results and the time-dependent RMSD (root-mean-square deviation) of the Li_2S crystal structure based on experimental data (Exp.). The calculated diffusion coefficients were $3.54 \times 10^{-6} \text{ cm}^2 \text{ s}^{-1}$, $9.37 \times 10^{-6} \text{ cm}^2 \text{ s}^{-1}$, and $1.351 \times 10^{-5} \text{ cm}^2 \text{ s}^{-1}$ at 300 K, 500 K, and 700 K, respectively (Figure S2b). These values are slightly higher than those obtained from theoretical calculations based on crystallographic databases, which can be attributed to the larger lattice parameter of the synthesized material. The Arrhenius plot of Li_2S (Exp.) at different temperatures is shown in Figure S2c, yielding an activation energy of 0.0609 eV. This value is lower than that derived from theoretical calculations, again due to the larger lattice parameter and cell volume of the experimental structure. MD simulations provide insights into the time-dependent ion dynamics of the Li_2S crystal structure, while the Nudged Elastic Band (NEB) method offers precise energy barriers for individual Li^+ hopping events. Together, these approaches are essential for identifying favorable conduction pathways and understanding ionic transport in Li_2S .

Fig. 9 shows the calculated activation energy map and Li^+ ion migration pathways in the Li_2S crystal structure, obtained using the Nudged Elastic Band (NEB) method. The local activation energy for lithium-ion hopping along transfer paths 1–3 was determined to be

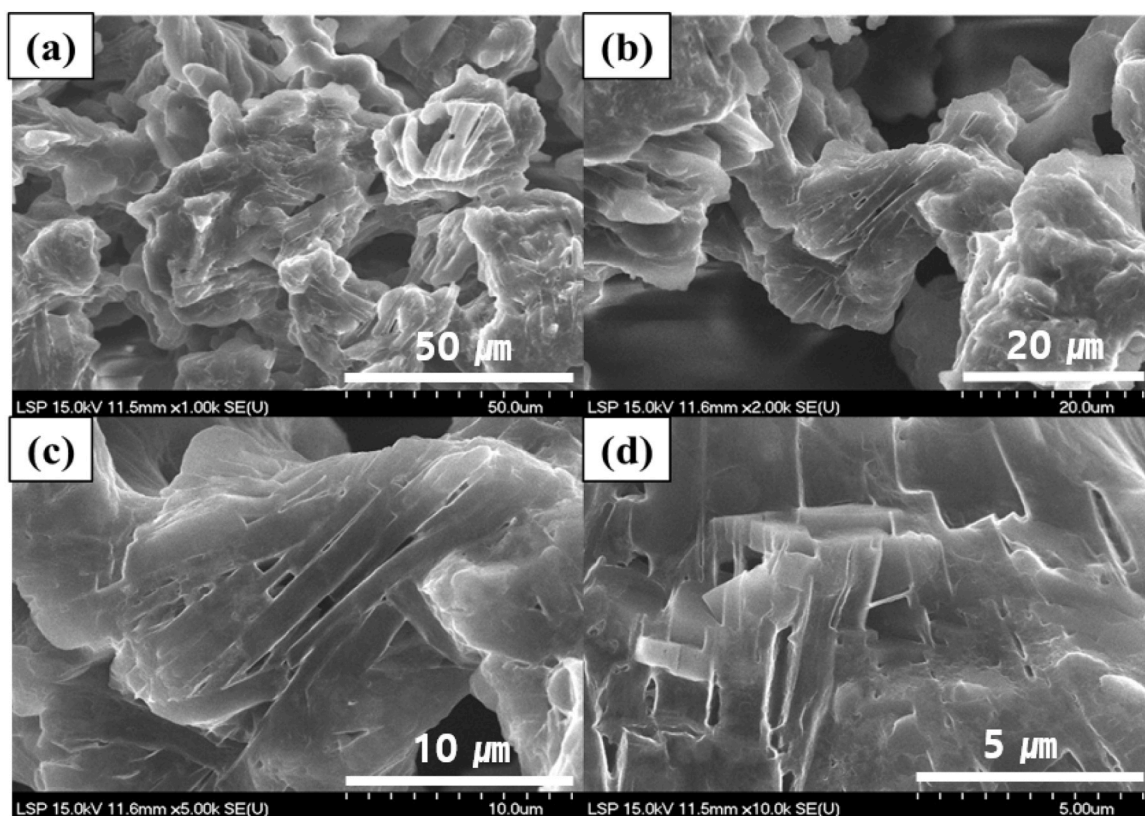


Fig. 4. (a-d) FE-SEM images of Li_2S particles at different magnifications.

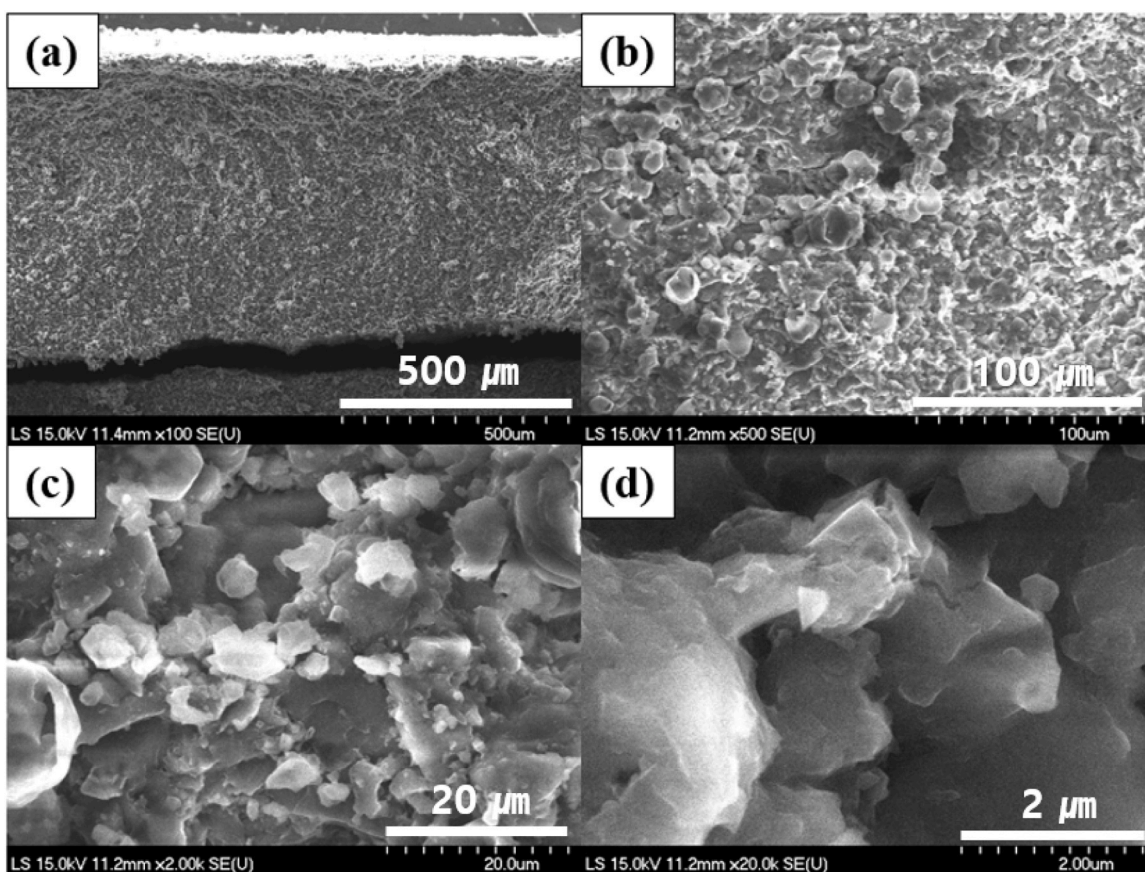


Fig. 5. (a-d) FE-SEM images of Li_2S pellet at different magnifications.

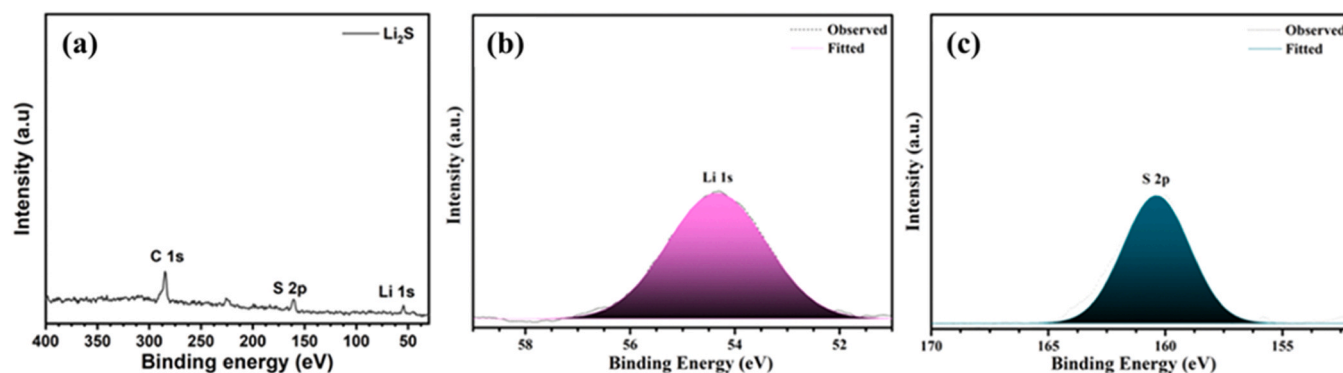


Fig. 6. XPS results of Li_2S prepared at 780 °C. (a) Full spectra (b) Li 1 s spectra and (c) S 2p spectra.

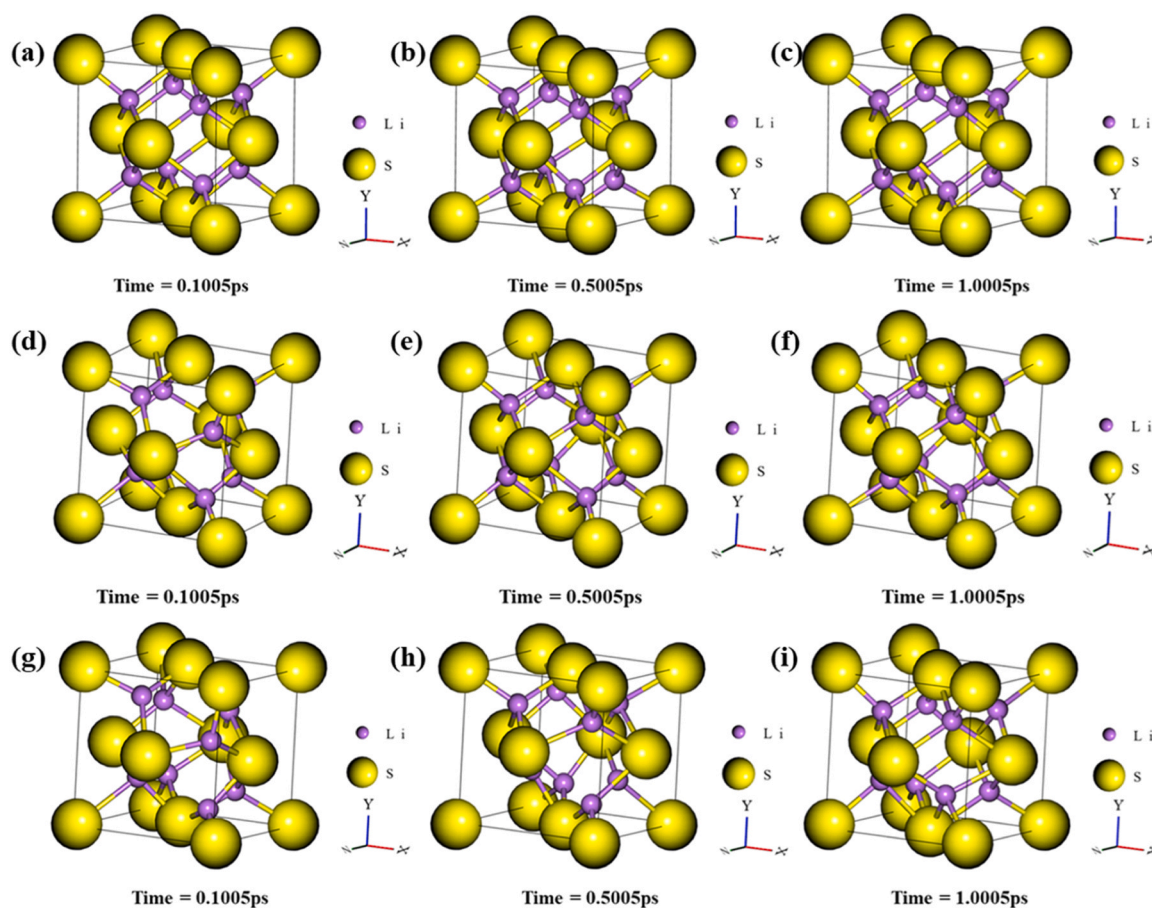


Fig. 7. Molecular Dynamics (MD) simulation results of Li_2S crystal structure under different temperatures at particular time. (a-c) 300 K, (d-f) 500 K and (g-i) 700 K.

0.396 eV. The corresponding hopping distances between lithium sites were 2.8352 Å for each of the following pathways: Li2–Li3 (path 1), Li4–Li5 (path 2), and Li6–Li7 (path 3). These findings provide valuable insights into the energy barriers associated with Li^+ transport and the feasibility of ion migration within the crystal lattice, supporting the material's potential as a solid-state ionic conductor.

Fig. 10 presents the calculated activation energy landscape and Li^+ ion hopping trajectories along transfer paths 4 through 7 in the Li_2S crystal structure, based on Nudged Elastic Band (NEB) calculations. The computed activation energy for each path—path 4 (Li1–Li2), path 5 (Li3–Li4), path 6 (Li5–Li6), and path 7 (Li7–Li8)—was found to be 1.056 eV. The corresponding hopping distance for all four pathways was 4.9107 Å. Importantly, the activation energies along these equivalent

lattice directions (x, y, and z) were nearly identical, indicating no directional anisotropy. This result suggests that Li_2S exhibits isotropic ionic conduction behavior, a favorable characteristic for its application in solid-state electrolyte systems.

Fig. 11 presents the NEB-calculated activation energy profile for lithium ion migration along transfer path 8 in the Li_2S crystal structure. The calculated activation energy for this pathway was 0.688 eV, with a corresponding hopping distance of 4.0095 Å between Li1 and Li3. This result, in conjunction with the data from previous pathways, further supports the conclusion that lithium ion diffusion in the Li_2S lattice is isotropic in nature, with comparable migration barriers across different crystallographic directions.

Additionally, the nudged elastic band (NEB) method was employed

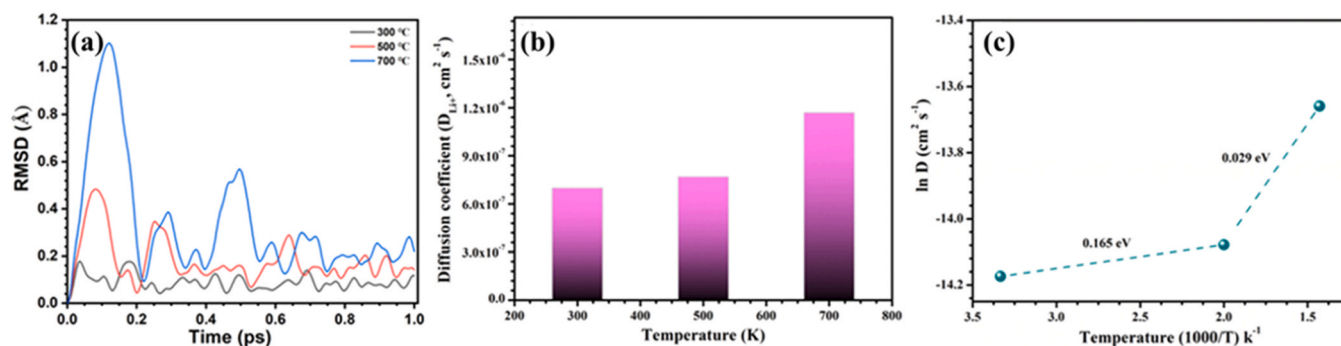


Fig. 8. (a) Time (ps) vs RMSD (Root mean square deviation, Å), (b) Temperature (K) vs Diffusion coefficient (D_{Li^+}), and (c) Arrhenius plot of the Li_2S pellet.

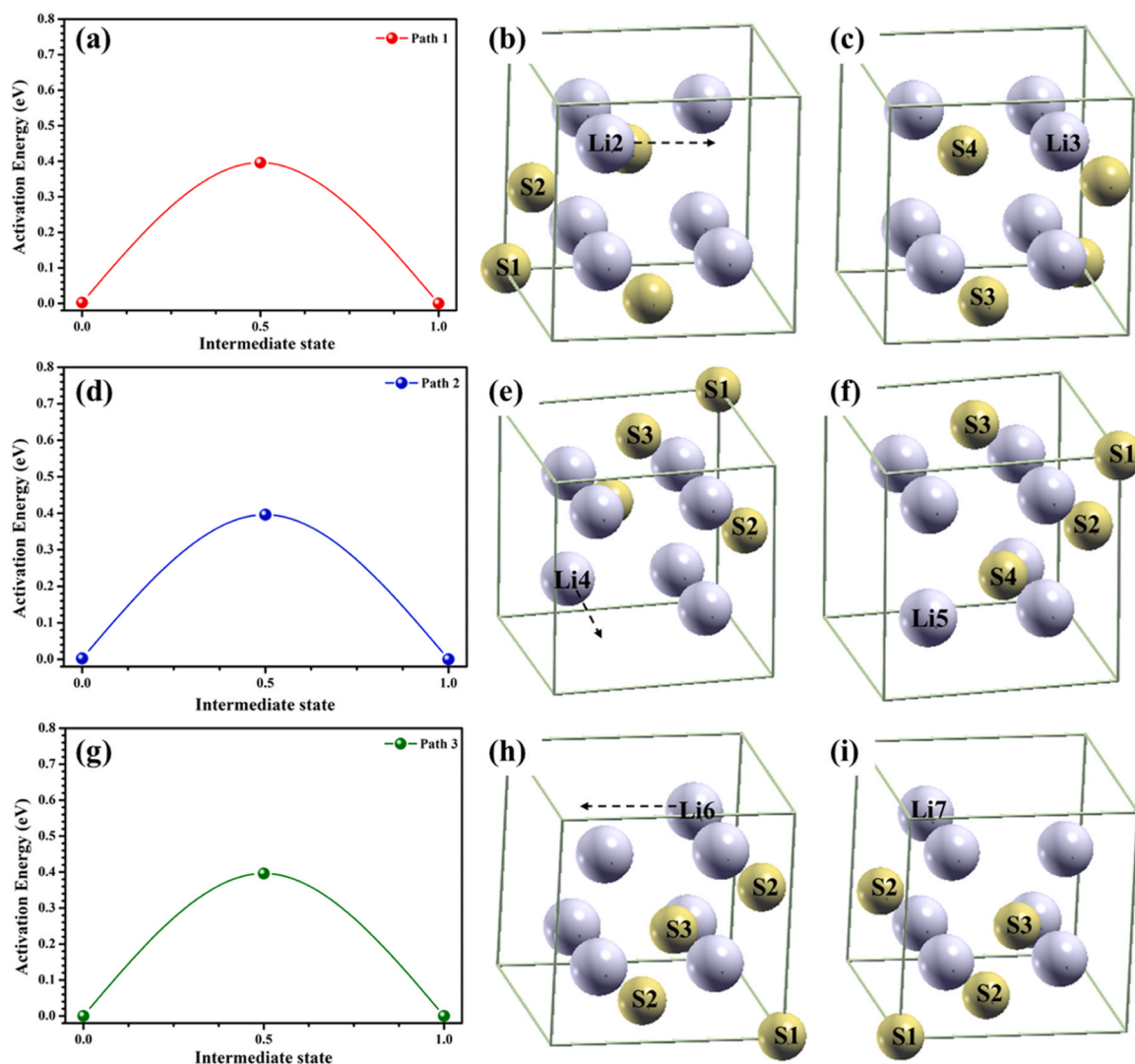


Fig. 9. Nudged Elastic band (NEB) was used to calculate the activation energy for lithium ion hopping at different site. (a-c) Ion transfer path 1, (d-f) Ion transfer path 2 and (g-i) Ion transfer path 3.

to calculate the local activation energy (E_{Li}^{\ddagger}) of the Li_2S crystal structure (Exp.). Figure S3 presents the activation energy map together with the ion-hopping pathways at different sites. The calculated activation energies for paths 1, 6, and 8 were 0.261 eV, 1.069 eV, and 0.788 eV, respectively. The corresponding Li–Li distances were 2.8544 Å (Li2–Li3), 4.9439 Å (Li1–Li2), and 4.0367 Å (Li1–Li3). Overall, the NEB results for the Li_2S crystal (Exp.) show good agreement with the

theoretical NEB calculations.

Fig. 12(a) presents the atomic configuration of lithium (Li) and sulfur (S) ions in the Li_2S crystal structure, illustrating their occupation of specific lattice sites. Lithium ions are positioned at the 8c Wyckoff sites, while sulfur ions occupy the 4a sites within a face-centered cubic (FCC) lattice. Fig. 12(b) shows a three-dimensional electron density map obtained from Density Functional Theory (DFT) calculations, depicting the

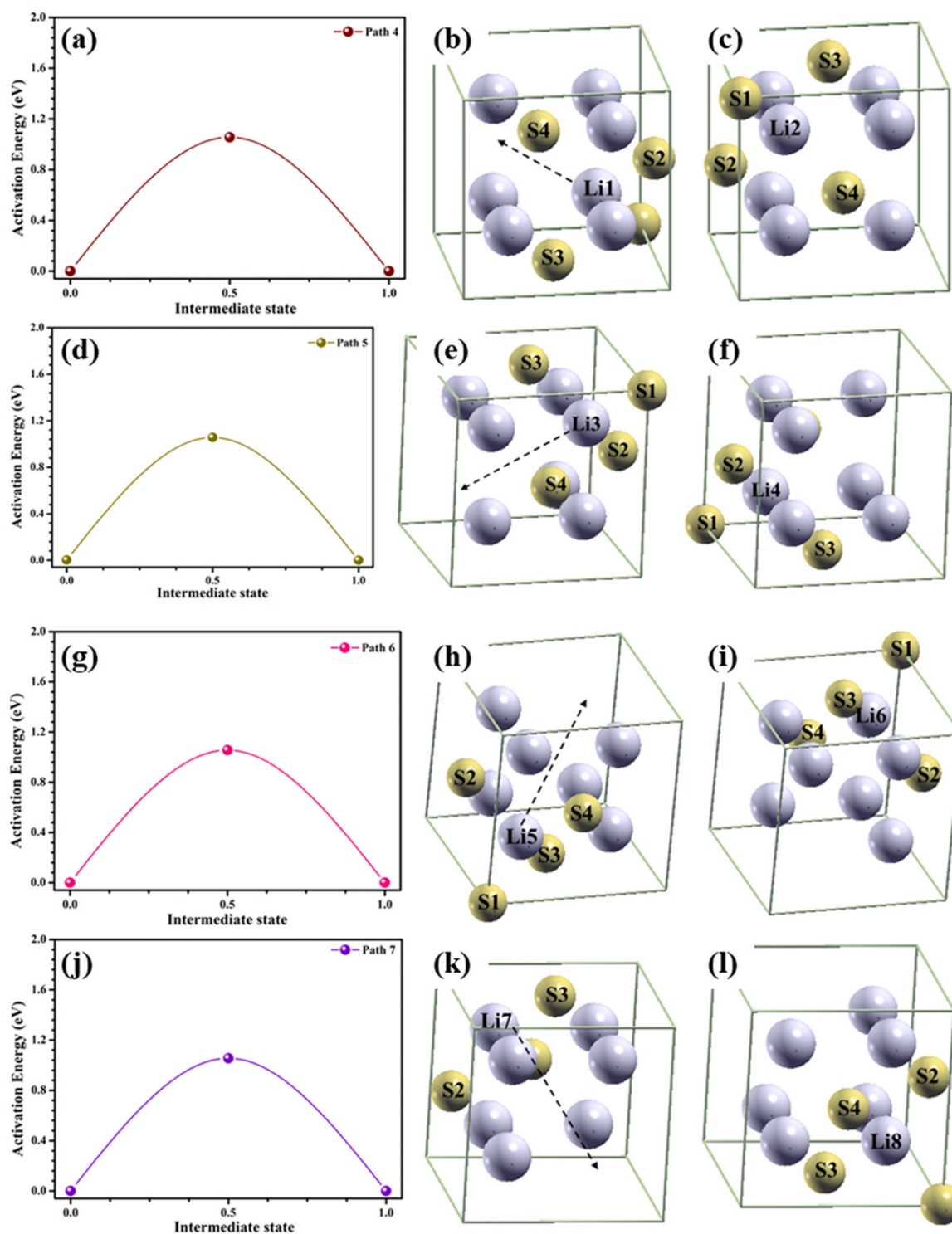


Fig. 10. Nudged Elastic band (NEB) was used to calculate the activation energy for lithium ion hopping at different site. (a-c) Ion transfer path 4, (d-f) Ion transfer path 5, (g-i) Ion transfer path 6 and (j-l) Ion transfer path 7.

spatial distribution of electronic charge around Li and S atoms. The isosurface visualization reveals regions of high electron density surrounding sulfur atoms and lower density near lithium sites, consistent with their respective electronegativities. Furthermore, the electron density contours suggest potential Li^+ ion migration pathways, supporting the isotropic conduction behavior of lithium ions within the Li_2S lattice.

Fig. 13 displays the EIS spectra of the Li_2S pellet at 60 °C and 80 °C. The resistance value decreased as the working temperature increased

due to faster ion transfer. The calculated ionic conductivity of the pellet was $2.44 \times 10^{-6} \text{ S cm}^{-1}$ and $6.39 \times 10^{-6} \text{ S cm}^{-1}$, values considerably higher than those reported in previous studies [4,48]. In the future, we plan to prepare Lithium sulfur solid electrolytes using this precursor material. Overall, our findings suggest an economical approach to synthesize cubic Li_2S precursor powder and enhance understanding of the ion conduction mechanism in the crystal structure.

Fig. 13 displays the EIS spectra of the Li_2S pellet at 60 °C and 80 °C. The resistance value decreased as the working temperature increased

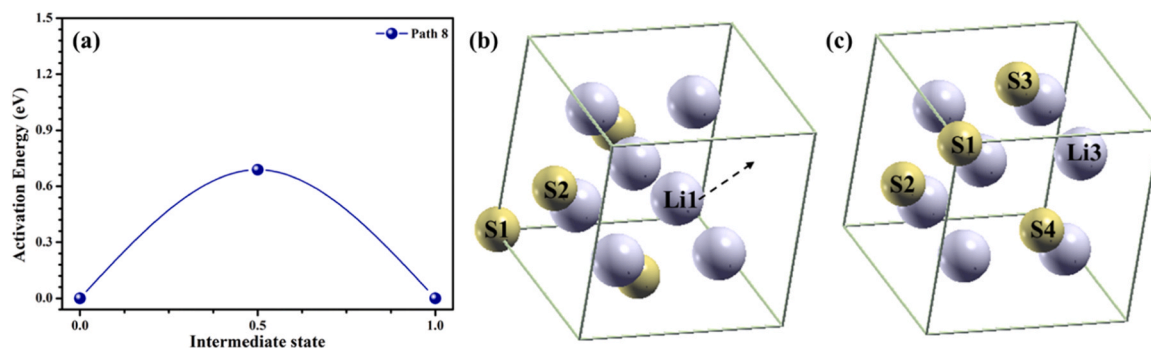


Fig. 11. Nudged Elastic band (NEB) was used to calculate the activation energy for lithium ion hopping at different site. (a-c) Ion transfer path 8.

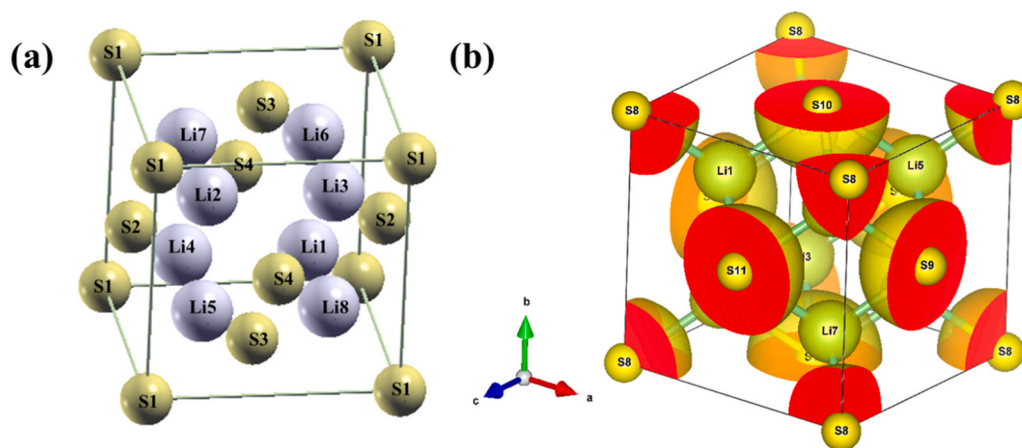


Fig. 12. (a) Lithium and Sulfur ions position at different sites and (b) 3D- Electron density map of the DFT calculated Li_2S crystal structure.

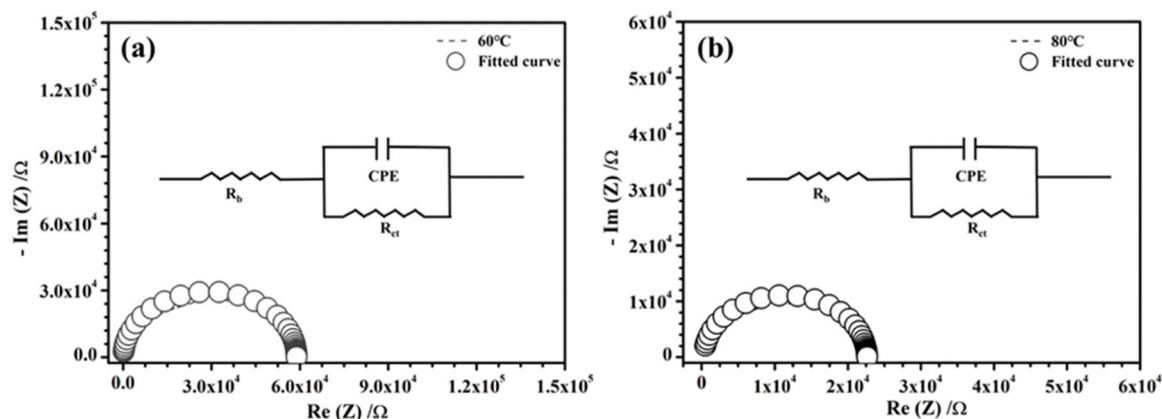


Fig. 13. EIS results of the Li_2S pellets at particular temperatures. (a) 60 °C and (b) 80 °C.

due to faster ion transfer. The calculated ionic conductivity of the pellet was $2.44 \times 10^{-6} \text{ S cm}^{-1}$ and $6.39 \times 10^{-6} \text{ S cm}^{-1}$, values considerably higher than those reported in previous studies [4,48]. The equivalent circuit $R_0 + (\text{CPE}/R_{ct})$ represents a typical *Randles* circuit model, where R_0 corresponds to the bulk (ohmic) resistance, and the parallel combination of a Constant Phase Element (CPE) and the charge-transfer resistance (R_{ct}) represents the Faradaic impedance at the grain boundary [49]. Following Li^+ conductivity, the Li-ion transference number is a key parameter for Li-ion conductors, as it directly influences Li-ion transport efficiency, and cell electrochemical performance. Figures S4 and S5 present the EIS spectra and chronoamperometry results of the ion-blocking $\text{In}/\text{Li}_2\text{S}/\text{Li}$ and non-ion-blocking $\text{Li}/\text{Li}_2\text{S}/\text{Li}$ symmetric

cells at 60 °C and 80 °C, respectively.

The Li^+ transference number (t_{Li}^+) of the Li_2S crystal was calculated using the following equation: [50,51]

$$t_{\text{Li}}^+ = \frac{i_s(\Delta V - i_0 R_0)}{i_0(\Delta V - i_s R_s)}$$

In the above equation, i_0 and i_s represent the initial and steady-state currents, respectively; V denotes the polarization voltage; R_0 and R_s correspond to the sum of the charge-transfer resistance R_{ct} and R_{film} represents the passivation film resistance. The AC impedance spectra in the frequency range of 7 MHz to 100 Hz were used to determine R_s and R_0 of the cell. Polarization measurements were carried out using $\text{In}/$

Li₂S//Li and Li//Li₂S//Li symmetric cells under a DC voltage (ΔV) of 1 V at 60 °C and 80 °C until steady state was achieved. Table S1 summarizes the data obtained from electrochemical studies of Li₂S using ion-blocking indium and non-ion-blocking lithium symmetric cells. The Li-ion transference numbers for Li₂S were determined to be 0.96 and 0.98 at 60 °C and 80 °C, respectively (Table S1). These results indicate that the presence of carbon slightly reduces the Li-ion transference number of the Li₂S pellet. In the future, we plan to prepare Lithium sulfur solid electrolytes using this precursor material. Overall, our findings suggest an economical approach to synthesize cubic Li₂S precursor powder and enhance understanding of the ion conduction mechanism in the crystal structure.

4. Conclusion

The cubic-phase Li₂S crystal structure was successfully synthesized via a cost-effective carbothermal reduction method. Theoretical analyses confirmed the atomic positions of lithium and sulfur ions and provided insights into the lithium ion transport pathways within the lattice. Electrochemical impedance spectroscopy (EIS) revealed ionic conductivities of $2.44 \times 10^{-6} \text{ S cm}^{-1}$ at 60 °C and $6.39 \times 10^{-6} \text{ S cm}^{-1}$ at 80 °C, indicating promising ion transport characteristics. Molecular dynamics (MD) simulations further demonstrated enhanced ionic behavior at elevated temperatures, particularly at 700 °C. Additionally, Nudged Elastic Band (NEB) calculations identified feasible Li⁺ migration pathways and estimated activation energies, supporting the potential of isotropic ion conduction in Li₂S. Collectively, these findings offer valuable insights into the ion conduction mechanism and demonstrate the viability of Li₂S as a precursor material for next-generation lithium-sulfur solid-state electrolytes.

Declaration of Competing Interest

The authors declare that they have no known competing financial interests or personal relationships that could have appeared to influence the work reported in this paper

Acknowledgments

This research was financially supported by the Ministry of Trade, Industry and Energy, Korea, under the “Regional Innovation Cluster Development Program(R&D, P0025257)” supervised by the Korea Institute for Advancement of Technology(KIAT).

Appendix A. Supporting information

Supplementary data associated with this article can be found in the online version at doi:10.1016/j.nxmte.2025.101305.

References

- [1] B. Ramkumar, K. So-young, N. Chan-woo, V. Aravindan, Y.S. Lee, LiBO₂-modified LiCoO₂ as an efficient cathode with garnet framework Li_{6.75}La₃Zr_{1.75}Nb_{0.25}O₁₂ electrolyte toward building all-solid-state lithium battery for high-temperature operation, *Electro Acta* 359 (2020) 136955, <https://doi.org/10.1016/j.electacta.2020.136955>.
- [2] B. Ramkumar, C. Nam, V. Aravindan, D. Eum, K. Kang, Y.S. Lee, Interfacial engineering in a cathode composite based on Garnet-Type Solid-State Li-Ion battery with high voltage cycling, *ChemElectroChem* 8 (3) (2021) 570–576, <https://doi.org/10.1002/celec.202001116>.
- [3] B. Ramkumar, V. Aravindan, H. Ramasamy, K.V. Ajeya, J.G. Ryu, H.Y. Jung, Y. S. Lee, Ternary metal oxide filled PEO-based polymer electrolyte for solid-state lithium metal battery: the role of filler particle size, *Solid State Sci.* 132 (2022) 106958, <https://doi.org/10.1016/j.solidstatesciences.2022.106958>.
- [4] S. Luo, F. Wu, G. Yushin, Strategies for fabrication, confinement and performance boost of Li₂S in lithium-sulfur, silicon-sulfur & related batteries, *Mater. Today* 49 (2021) 253–270, <https://doi.org/10.1016/j.mattod.2021.03.017>.
- [5] R. Balasubramaniam, C.W. Nam, V. Aravindan, J.C. Seol, K.V. Ajeya, H.Y. Jung, Y. S. Lee, Composite solid electrolyte for high voltage Solid-State Li-Metal battery, *ChemElectroChem* 9 (2022) e202200317, <https://doi.org/10.1002/celec.202200317>.
- [6] F. Thomas, L. Mahdi, J. Lemaire, D.M.F. Santos, Technological advances and market developments of solid-state batteries: a review, *Materials* 17 (2024) 239, <https://doi.org/10.3390/ma17010239>.
- [7] Y. Liu, X. Meng, Z. Wang, J. Qiu, A Li₂S-based all-solid-state battery with high energy and superior safety, *Sci. Adv.* 8 (2022) eabl8390, <https://doi.org/10.1126/sciadv.abl8390>.
- [8] Y. Nikodimos, C.J. Huang, B.W. Taklu, W.N. Su, B.J. Hwang, Chemical stability of sulfide solid-state electrolytes: stability toward humid air and compatibility with solvents and binders, *Energy Environ. Sci.* 15 (2022) 991–1033, <https://doi.org/10.1039/d1ee03032a>.
- [9] W.G. Suci, H.K. Aliwarga, Y.R. Azinuddin, R.B. Setyawati, K.N.R. Stulasti, A. Purwanto, Review of various sulfide electrolyte types for solid-state lithium-ion batteries, *Open Eng.* 12 (2022) 409–423, <https://doi.org/10.1515/eng-2022-0043>.
- [10] W.G. Suci, H.K. Aliwarga, Y.R. Azinuddin, R.B. Setyawati, K.N.R. Stulasti, A. Purwanto, Review of various sulfide electrolyte types for solid-state lithium-ion batteries, *Open Eng.* 12 (2022) 409–423. doi:10.1515/eng-2022-0043.
- [11] M.V. Reddy, C.M. Julien, A. Mauger, K. Zaghib, Sulfide and oxide inorganic solid electrolytes for all-solid-state Li batteries: a review, *Nanomaterials* 10 (2020) 1606, <https://doi.org/10.3390/nano10081606>.
- [12] Y. Zhao, W. Smith, C.A. Wolden, Scalable synthesis of Li₂S nanocrystals for Solid-State electrolyte applications, *J. Electrochem Soc.* 167 (2020) 070520, <https://doi.org/10.1149/1945-7111/ab6e3f>.
- [13] K. Yuan, L. Yuan, J. Chen, J. Methods and cost estimation for the synthesis of nanosized lithium sulfide, *Small Struct.* 2 (2021) 2000059, <https://doi.org/10.1002/ssstr.202000059>.
- [14] F. Wu, H. Kim, A. Magasinski, J.T. Lee, H.T. Lin, G. Yushin, Harnessing steric separation of freshly nucleated Li₂S nanoparticles for bottom-up assembly of high-performance cathodes for lithium-sulfur and lithium-ion batteries, *Adv. Energy Mater.* 4 (2014) 1400196, <https://doi.org/10.1002/aenm.201400196>.
- [15] X. Li, M. Gao, W. Du, B. Ni, Y. Wu, Y. Liu, C. Shang, Z. Guo, H. Pan, A mechanochemical synthesis of submicron-sized Li₂S and a mesoporous Li₂S/C hybrid for high performance lithium/sulfur battery cathodes, *J. Mater. Chem. A* 5 (2017) 6471–6482, <https://doi.org/10.1039/c7ta00557a>.
- [16] S. Virji, R.B. Kaner, B.H. Weiller, Direct electrical measurement of the conversion of metal acetates to metal sulfides by hydrogen sulfide, *Inorg. Chem.* 45 (2006) 10467–10471, <https://doi.org/10.1021/ic0607585>.
- [17] X. Li, C.A. Wolden, C. Ban, Y. Yang, Facile synthesis of lithium sulfide nanocrystals for use in advanced rechargeable batteries, *ACS Appl. Mater. Interfaces* 7 (2015) 28444–28451, <https://doi.org/10.1021/acsami.5b09367>.
- [18] X. Li, Y. Zhao, A. Brennan, M. McCeig, C.A. Wolden, Y. Yang, Reactive precipitation of anhydrous alkali sulfide nanocrystals with concomitant abatement of hydrogen sulfide and cogeneration of hydrogen, *ChemSusChem* 10 (2017) 2904–2913, <https://doi.org/10.1002/cssc.201700532>.
- [19] N. Hart, J. Shi, J. Zhang, C. Fu, J. Guo, Lithium sulfide-carbon composites via aerosol spray pyrolysis as cathode materials for lithium-sulfur batteries, *Front Chem.* 6 (2018) 476, <https://doi.org/10.3389/fchem.2018.00476>.
- [20] C.B. Dressel, H. Jha, A.M. Eberle, H.A. Gasteiger, T.F. Fässler, Electrochemical performance of lithium-sulfur batteries based on a sulfur cathode obtained by H₂S gas treatment of a lithium salt, *J. Power Sources* 307 (2016) 844–848, <https://doi.org/10.1016/j.jpowsour.2015.12.140>.
- [21] C. Nan, Z. Lin, H. Liao, M.K. Song, Y. Li, E.J. Cairns, Durable carbon-coated Li₂S core-shell spheres for high performance lithium/sulfur cells, *J. Am. Chem. Soc.* 136 (2014) 4659–4663, <https://doi.org/10.1021/ja412943h>.
- [22] Y. Wu, T. Momma, S. Ahn, T. Yokoshima, H. Nara, T. Osaka, On-site chemical pre-lithiation of s cathode at room temperature on a 3D nano-structured current collector, *J. Power Sources* 366 (2017) 65–71, <https://doi.org/10.1016/j.jpowsour.2017.08.113>.
- [23] L. Yin, W. Li, Q. Cao, S.W. Or, Z. Xing, The industrialization of lithium sulfide nanopowder material, *Chem* 10 (9) (2024) 2609–2614, <https://doi.org/10.1016/j.chempr.2024.07.023>.
- [24] W. Li, Q. Huang, Z. Li, Y. Wang, S.W. Or, S. Sun, Z. Xing, Lowered activation potential of lithium sulfide cathode material aided by electrolyte additive, *ACS Energy Lett.* 9 (2) (2024) 528–537, <https://doi.org/10.1021/acscenergylett.3c02551>.
- [25] J. Huang, W. Li, W. Zhang, B. Lin, Y. Wang, S.W. Or, S. Sun, Z. Xing, Lithium sulfide: a promising prelithiation agent for high-performance lithium-ion batteries, *SusMat* 4 (1) (2024) 34–47, <https://doi.org/10.1002/sus2.177>.
- [26] M. Kohl, J. Brückner, I. Bauer, H. Althues, S. Kaskel, Synthesis of highly electrochemically active Li₂S nanoparticles for lithium-sulfur-batteries, *J. Mater. Chem. A* 3 (2015) 16307–16312, <https://doi.org/10.1039/c5ta04504e>.
- [27] Y. Zhang, M.X. Xie, W. Zhang, J.L. Yan, G.Q. Shao, Synthesis and purification of SiS₂ and Li₂S for Li_{9.54}Si_{1.74}P_{1.44}S_{11.7}Cl_{0.3} solid electrolyte in Lithium-ion batteries, *Mater. Lett.* 266 (2020) 9–12, <https://doi.org/10.1016/j.matlet.2020.127508>.
- [28] J. Liu, H. Nara, T. Yokoshima, T. Momma, T. Osaka, Micro-scale Li₂S–C composite preparation from Li₂SO₄ for cathode of lithium ion battery, *Electrochim. Acta* 183 (2015) 70–77.
- [29] F. Ye, H. Noh, J. Lee, H. Lee, H.T. Kim, Li₂S/carbon nanocomposite strips from a lower-temperature conversion of Li₂SO₄ as high-performance lithium-sulfur cathodes, *J. Mater. Chem. A* 6 (2018) 6617–6624, <https://doi.org/10.1039/c8ta00515j>.
- [30] P. Giannozzi, S. Baroni, N. Bonini, M. Calandra, R. Car, C. Cavazzoni, D. Ceresoli, G.L. Chiarotti, M. Cococcioni, I. Dabo, A.D. Corso, S. Fabris, G. Fratesi, S. D. Gironcoli, R. Gebauer, U. Gerstmann, C. Gougousis, A. Kokalj, M. Lazzeri, L. M. Samos, A. Kokalj, M. Lazzeri, L.M. Samos, N. Marzari, F. Mauri, R. Mazzarello, S. Paolini, A. Pasquarello, L. Paulatto, C. Sbraccia, S. Scandolo, G. Sclauzero, A.

- P. Seitsonen, A. Smogunov, P. Umari, R.M. Wentzcovitch, QUANTUM ESPRESSO: a modular and open-source software project for quantum simulations of materials, *J. Phys. Condens Matter* 21 (39) (2009) 395502, <https://doi.org/10.1088/0953-8984/21/39/395502>.
- [30] S. Scandolo, P. Giannozzi, C. Cavazzoni, S.D. Gironcoli, A. Pasquarello, S. Baroni, First-principles codes for computational crystallography in the Quantum-ESPRESSO package, *Z. Krist.* 220 (2005) 574–579.
- [31] K.F. Garrity, J.W. Bennett, K.M. Rabe, D. Vanderbilt, Pseudopotentials for high-throughput DFT calculations, *Comput. Mater. Sci.* 81 (2014) 446–452, <https://doi.org/10.1016/j.commatsci.2013.08.053>.
- [32] G. Prandini, A. Marrazzo, I.E. Castelli, N. Mounet, N. Marzari, Precision and efficiency in solid-state pseudopotential calculations, *npj Comput. Mater.* 4 (2018) 72, <https://doi.org/10.1038/s41524-018-0127-2>.
- [33] E. Zintl, A. Harder, B. Dauth, Gitterstruktur der oxide, sulfide, selenide und telluride des lithiums, natriums und kaliums, *Z. F. ür. Elektrochem. und Angew. Phys. Chem.* 40 (1934) 588–593.
- [34] F. Altorfer, W. Buhner, I. Anderson, O. Scharpf, H. Bill, H.G. Smith, P.L. Carron, Structural and dynamical properties of Li_2S , *Solid State Ion. Proc. Symp. A2 Int. Conf. Adv. Mater.* (1991) 1991 (1992) 325–330.
- [35] R.W.G. Wyckoff, New York Anti-fluorite structure, in: *Crystal Structures*, second ed., 1, Interscience Publishers, New York, 1963, pp. 239–444.
- [36] W. Buehrer, F. Altorfer, J. Mesot, H. Bill, P. Carron, H.G. Smith, Lattice dynamics and the diffuse phase transition of lithium sulphide investigated by coherent neutron scattering, *J. Phys. Condens. Matter* 3 (1991) 1055–1064.
- [37] E. Zintl, A. Harder, B. Dauth, Gitterstruktur der oxide, sulfide, selenide und telluride des lithiums, natriums und kaliums, *Z. fuer Elektrochem.* 40 (1934) 588–593.
- [38] A. Claassen, The crystal structure of water free alkali monosulfides, *Recl. Des. Trav. Chim. Des. PaysBas Et. De. la Belg.* 44 (1925) 790–794.
- [39] K. Momma, F. Izumi, VESTA: a three-dimensional visualization system for electronic and structural analysis, *J. Appl. Crystallogr* 41 (3) (2008) 653–658, <https://doi.org/10.1107/S0021889808012016>.
- [40] K. Momma, F. Izumi, VESTA 3 for three-dimensional visualization of crystal, volumetric and morphology data, *J. Appl. Crystallogr* 44 (6) (2011) 1272–1276, <https://doi.org/10.1107/S0021889811038970>.
- [41] J.P. Perdew, K. Burke, M. Ernzerhof, Generalized gradient approximation made simple, *Phys. Rev. Lett.* 77 (1996) 3865–3868, <https://doi.org/10.1103/PhysRevLett.77.3865>.
- [42] H. Jonsson, G. Mills, K.W. Jacobsen, Nudged elastic band method for finding minimum energy paths of transitions, *Class. Quantum Dyn. Condens. phase Simul.* (1998) 385–404, https://doi.org/10.1142/9789812839664_0016.
- [43] S. Scandolo, P. Giannozzi, C. Cavazzoni, S. De Gironcoli, A. Pasquarello, S. Baroni, First-principles codes for computational crystallography in the Quantum-ESPRESSO package, *Z. fur Krist.* 220 (2005) 574–579, <https://doi.org/10.1524/zkri.220.5.574.65062>.
- [44] A. Kokalj, XCrysDen - a new program for displaying crystalline structures and electron densities, *J. Mole.Graphics and modelling* 17 (1999) 176–179, [https://doi.org/10.1016/S1093-3263\(99\)00028-5](https://doi.org/10.1016/S1093-3263(99)00028-5).
- [45] X. Li, X. Sun, Nitrogen-doped carbons in Li-S batteries: materials design and electrochemical mechanism, *Front Energy Res* 2 (2014) 49, <https://doi.org/10.3389/fenrg.2014.00049>.
- [46] Z. Lin, Z. Liu, N.J. Dudney, C. Liang, Lithium superionic sulfide cathode for all-solid lithium-sulfur batteries, *ACS Nano* 7 (3) (2013) 2829–2833, <https://doi.org/10.1021/nn400391h>.
- [47] H. Hareendrakrishnakumar, R. Chuliyote, M.G. Joseph, Ion-selective PEDOT:PSS-decorated separator as a potential polysulfide immobilizer for lithium-sulfur batteries, *Ion. (Kiel.)* 27 (3) (2021) 1087–1099, <https://doi.org/10.1007/s11581-020-03870-5>.
- [48] M. Xiao, W. Li, M. Yu, B. Lin, D. PEng, Z.Z. Li, S.W. Or, S. Sun, Z. Xing, Enhanced electronic conductivity and ionic conductivity of Li_2S by doping strategy 8 (3) (2025) 101934.
- [49] W. Choi, H.C. Shin, J.M. Kim, J.Y. Choi, W.S. Yoon, Modeling and applications of electrochemical impedance spectroscopy (Eis) for lithium-ion batteries, *J. Electrochem Sci. Technol.* 11 (1) (2020) 1–13, <https://doi.org/10.33961/jecst.2019.00528>.
- [50] M. Riley, P.S. Fedkiw, S.A. Khan, Transport properties of lithium Hectorite-Based composite electrolytes, *J. Electrochem Soc.* 149 (6) (2002) A667, <https://doi.org/10.1149/1.1470652>.
- [51] J. Zhao, L. Wang, X. He, C. Wan, C. Jiang, Determination of Lithium-Ion transference numbers in LiPF_6 -PC solutions based on electrochemical polarization and NMR measurements, *J. Electrochem Soc.* 155 (4) (2008) A292, <https://doi.org/10.1149/1.2837832>.